Neutron removal from the deformed halo nucleus ^{31}Ne

Juhee Hong,[1] C. A. Bertulani,[2] and A. T. Kruppa[3]
[1]*Rare Isotope Science Project, Institute for Basic Science, Daejeon 305-811, Korea*
[2]*Department of Physics, Texas A&M University-Commerce, Commerce, Texas 75429, USA*
[3]*Institute for Nuclear Research, Hungarian Academy of Sciences, P.O. Box 51, H-4001 Debrecen, Hungary*
(Received 7 April 2017; revised manuscript received 9 October 2017; published 5 December 2017)

Experimental data on Coulomb breakup and neutron removal indicate that ^{31}Ne is one of the heaviest halo nuclei discovered so far. The possible ground state of ^{31}Ne is either $3/2^-$ coming from the p-wave halo or $1/2^+$ coming from the s-wave halo. In this work, we develop a treatable model to include deformed wave functions and a dynamical knockout formalism that includes the dependence on the nuclear orientation to study the neutron removal from ^{31}Ne projectiles at energies around $E \approx 200$ MeV/nucleon. A detailed account of the effects of deformation on cross sections and longitudinal momentum distributions is made. Our numerical analysis indicates a preference for the ^{31}Ne ground state with spin-parity $3/2^-$.

DOI: 10.1103/PhysRevC.96.064603

I. INTRODUCTION

The neutron-rich ^{31}Ne nucleus is expected to be strongly deformed with the pf-intruder configuration near the island of inversion. Its halo structure is relevant because it is one of the heaviest halo nuclei discovered so far [1]. The known data seem to indicate a mixing of valence spherical orbitals due to deformation. The valence neutron of ^{31}Ne is found to be in $2p_{3/2}$ or in $2s_{1/2}$, but not in $1f_{7/2}$ which is expected from the standard shell model [2–11]. There are also uncertainties in the deformation and the neutron binding energy for two possible ground spin-parity states.

In Ref. [12], the measured large Coulomb breakup cross section of ^{31}Ne was interpreted simply in terms of a p-wave neutron halo together with the deformed core. Hamamoto [12] suggests that the ground state of ^{31}Ne has either the spin-parity $1/2^+$ with a neutron separation energy of $S_n > 0.5$ MeV and a quadrupole deformation of $\beta_2 \gtrsim 0.59$ or the spin-parity $3/2^-$ with $S_n < 0.5$ MeV. The $1/2^+$ assignment arises from the Nilsson level [200 1/2] while the $3/2^-$ assignment is due to either (1) the [321 3/2] Nilsson level with $S_n < 0.2$ MeV and $0.40 \lesssim \beta_2 \lesssim 0.59$ or (2) the [330 1/2] level with $0.2\,\text{MeV} < S_n < 0.5$ MeV and $0.22 \lesssim \beta_2 \lesssim 0.30$.

In this work we consider one-neutron removal reactions as a probe of deformation and calculate cross sections and longitudinal momentum distributions with respect to the incident beam direction. We use a modified version of the Glauber model developed in Ref. [13] and extensively used in the literature [14–16]. In this model, a few approximations are made. It is assumed that the excitation energy of the relative motion between the core and the removed neutron is much smaller than the projectile energy and is neglected. This adiabatic condition is well satisfied for collisions on a light target with projectiles at intermediate energies ($E_{\text{lab}} \gtrsim 50$ MeV/nucleon). In the spectator-core approximation, the core can be at most elastically scattered by the target. With these assumptions, the shape of the momentum distribution of the core can be used to determine the degree of deformation of projectiles, the angular momentum content, and the binding energy of a valence nucleon. As an example, we show that these distributions can be used to identify the spin-parity of the ground state of ^{31}Ne.

Theoretical studies of nucleon removal reactions from deformed projectiles have been reported previously [11,17–21] and the longitudinal momentum distribution of stripping reactions has been calculated by using the Nilsson model. Glauber-type deformed potential S matrices have been used in Ref. [17], and the core-target S matrix has been calculated in the absorbing-disk approximation [22] in Ref. [20]. In this work, we calculate the momentum distribution with orientation-dependent S matrices obtained by the nuclear ground-state densities and the nucleon-nucleon cross section [23–25]. Orientation dependence is important because the valence nucleon knockout depends on the angle between the intrinsic deformation axis and the beam axis. The deformed states used in our calculations are obtained by a solution of coupled equations for a deformed Woods-Saxon potential. The approach is superior to the Nilsson model because the harmonic oscillator wave functions used in the model decay too fast at long distances and the asymptotic behavior of the Nilsson states is not correct. This is of relevance for reactions induced by halo nuclei, such as ^{31}Ne.

In Sec. II, we discuss nucleon removal reactions from deformed projectiles in an extension of the Glauber model of Ref. [13] to include deformation. We apply this formalism to study one-neutron removal reactions from deformed ^{31}Ne in Sec. III. The longitudinal momentum distributions and the total cross sections are then considered as functions of quadrupole deformation and neutron binding energy. By including spherical calculations for neutron removal from the core to populate excited core states, the inclusive momentum distributions are compared with experimental data. Finally, we summarize our results in Sec. IV.

II. NUCLEON REMOVAL FROM DEFORMED PROJECTILES

We consider single-nucleon removal reactions from a two-body composite projectile consisting of a core and a

valence nucleon. In our model, the nucleon removal reactions have contributions from two processes: diffraction dissociation and stripping [13,26]. Diffraction dissociation is the elastic breakup process in which a valence nucleon is separated from the core whereas the target remains in its ground state. In the stripping or absorption process, the removed nucleon reacts with the target and the target is excited. In nucleon removal from halo nuclei, the momentum distribution becomes narrow due to the large spatial extension of their intrinsic wave functions. Thus, it is useful to interpret the distribution in terms of the momentum-space wave function of the halo nuclei. Using the Glauber model [13,26], the nucleon removal under a spherical potential has been discussed by several authors, e.g., in Refs. [14–16]. In our work, the momentum distribution and the cross sections of stripping and diffraction dissociation are calculated with an extended version of the numerical code MOMDIS [15] to accommodate the changes described below. In the next subsections, we show how we include the projectile deformation in the nucleon removal cross sections in reactions with a spherical target.

A. Deformed states

To obtain the projectile deformed states, we use an updated version of the numerical code PSEUDO [27]. In the single-particle model for a deformed potential with axial symmetry, we have

$$V(\boldsymbol{r},\hat{\boldsymbol{\Omega}}) = \sum_{\lambda=0,2,4,\ldots} V_\lambda(r) Y_{\lambda 0}(\hat{\boldsymbol{\Omega}}), \tag{1}$$

and the ground state can be written as

$$\Psi_\omega(\boldsymbol{r},\hat{\boldsymbol{\Omega}}) = \sum_{\alpha,m,s_z} \left\langle lm\frac{1}{2}s_z \middle| j\omega\right\rangle \frac{u_{\alpha\omega}(r)}{r} Y_{lm}(\hat{\boldsymbol{\Omega}})\chi_{\frac{1}{2}s_z}, \tag{2}$$

where $\alpha = \{l,j\}$ and $\hat{\boldsymbol{\Omega}}$ defines the orientation of the symmetry axis relative to the laboratory system. The radial wave function is obtained by solving the following coupled system of ordinary differential equations:

$$-\frac{\hbar^2}{2\mu}\left[\frac{d^2}{dr^2} - \frac{l_\alpha(l_\alpha+1)}{r^2}\right]u_{\alpha\omega}(r) + \sum_{\alpha',\lambda}\left[V_{\alpha\alpha'\lambda}(r) + \frac{1}{r}V^{\rm sing}_{\alpha\alpha'\lambda}(r)\right]u_{\alpha'\omega}(r) = E u_{\alpha\omega}(r), \tag{3}$$

where $V_{\alpha\alpha'\lambda}$ is the potential component corresponding to the coupling between $\alpha = \{l,j\}$ and $\alpha' = \{l',j'\}$ channels in the presence of deformation β_λ, and $V^{\rm sing}_{\alpha\alpha'\lambda}(r)/r$ corresponds to the singular part (such as spin-orbit interaction) of the potential, which requires a special numerical treatment. In the present work, we consider quadrupole deformation ($\lambda = 2$) only.

The potential consists of the nuclear potential and the Coulomb potential. By expanding a deformed Woods-Saxon form factor with $R(\hat{\boldsymbol{\Omega}}) = R_0[1 + \sum_\lambda \beta_\lambda Y_{\lambda 0}(\hat{\boldsymbol{\Omega}})]$ (β_λ is the deformation parameter) and keeping only linear orders of deformation, the nuclear potential is given by

$$V_N(\boldsymbol{r},\hat{\boldsymbol{\Omega}}) = -V_0 f(r) - V_{SO}\left(\frac{\hbar}{m_\pi c}\right)^2 \frac{1}{r}\frac{df(r)}{dr}\boldsymbol{l}\cdot\boldsymbol{s} + V_0 R_0 \frac{df}{dr}\sum_\lambda \beta_\lambda Y_{\lambda 0}(\hat{\boldsymbol{\Omega}}), \tag{4}$$

where $f(r)$ is a spherical Woods-Saxon form factor and $\hbar/(m_\pi c) = 1.414$ fm is the pion Compton wavelength. The potential depths are adjusted to reproduce the ground-state energy. The Coulomb potential is parametrized as

$$V_C(\boldsymbol{r},\hat{\boldsymbol{\Omega}}) = \frac{Z_1 Z_2 e^2}{r}\theta(r-R_C) + \frac{Z_1 Z_2 e^2}{2R_C} \times \left(3 - \frac{r^2}{R_C^2}\right)\theta(R_C - r) + \sum_\lambda \frac{3Z_1 Z_2 e^2}{2\lambda+1} \times \left[\frac{R_C^\lambda}{r^{\lambda+1}}\theta(r-R_c) + \frac{r^\lambda}{R_C^{\lambda+1}}\theta(R_C - r)\right]\beta_\lambda Y_{\lambda 0}(\hat{\boldsymbol{\Omega}}), \tag{5}$$

where R_c is the Coulomb radius and $\theta(r)$ is the unit step function. For the case of ^{31}Ne (^{30}Ne $+ n$), the Coulomb potential has no influence in the calculations. For more details, see Ref. [27].

The basis functions are expressed in the projectile body-fixed frame with the $\hat{z}'$ axis along the core symmetry axis. Thus, we need to project them (with ω') on the laboratory coordinate system with the $\hat{z}$ axis along the beam direction:

$$\Psi_\omega(\boldsymbol{r},\hat{\boldsymbol{\Omega}}) = \sum_{\omega'} D^j_{\omega'\omega}(\hat{\boldsymbol{\Omega}})\,\Psi_{\omega'}(\boldsymbol{r}), \tag{6}$$

where $D^j_{\omega'\omega}(\hat{\boldsymbol{\Omega}})$ is the Wigner D matrix with the Euler angles $\hat{\boldsymbol{\Omega}} = (\phi_o,\theta_o,0)$.

B. Reaction S matrix

In the eikonal approximation, the S matrix is given by $S(\boldsymbol{b}) = \exp[i\chi(\boldsymbol{b})]$, with

$$\chi(\boldsymbol{b}) = -\frac{1}{\hbar v}\int dz V(\boldsymbol{b} + z\hat{\boldsymbol{z}}), \tag{7}$$

where v is the beam velocity along the $\hat{z}$ axis, and $V(\boldsymbol{b} + z\hat{\boldsymbol{z}})$ is the optical potential for core-target or nucleon-target interaction. The eikonal phase is obtained from the nuclear ground-state densities [23,24] as

$$\chi(\boldsymbol{b},\hat{\boldsymbol{\Omega}}) = \frac{1}{2\pi k_{NN}}\int d^3\boldsymbol{r} d^3\boldsymbol{r}'\rho_p(\boldsymbol{r},\hat{\boldsymbol{\Omega}})\rho_t(\boldsymbol{r}') \times \int d^2\boldsymbol{q} f_{NN}(\boldsymbol{q}) e^{-i(\boldsymbol{b}-\boldsymbol{\rho}-\boldsymbol{\rho}')\cdot\boldsymbol{q}}, \tag{8}$$

where k_{NN} is the nucleon-nucleon collision wave number, $\rho_p(\boldsymbol{r})$ [$\rho_t(\boldsymbol{r}')$] is the nuclear density of the projectile (target), and $f_{NN}(\boldsymbol{q})$ is the high-energy nucleon-nucleon scattering amplitude at forward angles. Assuming a spherical projectile

or an orientation-independent S matrix, the eikonal phase is

$$\chi_{\rm sph}(b) = \frac{1}{k_{NN}} \int dq q \rho_p(q) \rho_t(q) f_{NN}(q) J_0(qb), \quad (9)$$

where we have taken the Fourier transform of the densities.

For a deformed core, we expand the core density to linear orders of deformation [28]:

$$\rho_c(\boldsymbol{r}, \hat{\boldsymbol{\Omega}}) = \rho_c(r) + R_0 \sum_\lambda \beta_\lambda Y_{\lambda 0}(\hat{\boldsymbol{\Omega}}) \frac{\partial \rho_c}{\partial r}\bigg|_{\beta_\lambda = 0}. \quad (10)$$

Here, the spherical harmonics need to be rotated into the laboratory frame, $Y_{\lambda 0}(\hat{\boldsymbol{\Omega}}) = \sum_m D^\lambda_{m0}(\hat{\boldsymbol{\Omega}}) Y_{\lambda m}(\hat{\boldsymbol{r}})$. The eikonal phase of the core-target S matrix is then given by

$$\begin{aligned}\chi_{\rm def}(b, \hat{\boldsymbol{\Omega}}) = {} & \frac{1}{k_{NN}} \int dq\, q \rho_c(q) \rho_t(q) f_{NN}(q) J_0(qb) \\ & + \sum_{\lambda, m} R_0 \beta_\lambda D^\lambda_{m0}(\hat{\boldsymbol{\Omega}}) \int d^3\boldsymbol{r}\, Y_{\lambda m}(\hat{\boldsymbol{r}}) \frac{\partial \rho_c}{\partial r}\bigg|_{\beta_\lambda = 0} \\ & \times \frac{1}{2\pi k_{NN}} \int d^2\boldsymbol{q}\, \rho_t(q) f_{NN}(q) e^{-i(\boldsymbol{b}-\boldsymbol{\rho})\cdot\boldsymbol{q}}. \end{aligned} \quad (11)$$

For the quadrupole deformed core, we obtain (see the Appendix)

$$\begin{aligned}\chi_{\rm def}(b, \hat{\boldsymbol{\Omega}}) = {} & \frac{1}{k_{NN}} \int dq\, q \rho_c(q) \rho_t(q) f_{NN}(q) J_0(qb) \\ & + \frac{\sqrt{5\pi}}{k_{NN}} R_0 \beta_2 D^2_{00}(\hat{\boldsymbol{\Omega}}) \int dr \frac{\partial \rho_c}{\partial r}\bigg|_{\beta_2 = 0} \int dq\, J_0(qb) \rho_t(q) f_{NN}(q) \frac{1}{q^2 r} [(3 - q^2 r^2) \sin(qr) - 3qr \cos(qr)] \\ & + \sqrt{\frac{15\pi}{2}} \frac{1}{k_{NN}} R_0 \beta_2 \left[D^2_{20}(\hat{\boldsymbol{\Omega}}) + D^2_{-20}(\hat{\boldsymbol{\Omega}}) \right] \int dr\, \frac{\partial \rho_c}{\partial r}\bigg|_{\beta_2 = 0} \\ & \times \int dq\, J_2(qb) \rho_t(q) f_{NN}(q) \frac{1}{q^2 r} [(3 - q^2 r^2) \sin(qr) - 3qr \cos(qr)]. \end{aligned} \quad (12)$$

The core and target densities are obtained using the liquid-drop model [29]. We also include the effect of the nucleon size. For a valence nucleon, we use a Gaussian form of density given by $\exp[-(r/0.7)^2]$. The nucleon-nucleon scattering amplitude, $f_{NN}(q)$, is parametrized as [25]

$$f_{NN}(q) = \frac{k_{NN} \sigma_{NN}}{4\pi} (i + \alpha_{NN}) e^{-\beta_{NN} q^2}, \quad (13)$$

where σ_{NN}, α_{NN}, and β_{NN} are obtained by fitting the nucleon-nucleon scattering data.

C. Cross sections

The basic assumption in the application of the Glauber theory to stripping reactions is that one can write the cross sections as integrals over the transverse coordinates, and the impact parameter dependent S matrix can be interpreted as a survival probability [26]. In nucleon removal reactions, the core reaches a detector intact (with the probability $|S_c|^2$) and the valence nucleon is absorbed by the target (with $1 - |S_n|^2$, where S_c and S_n are the core-target and nucleon-target S matrices, respectively) [13,26].

For unpolarized projectile beams, we need to average over all orientations. Thus, the longitudinal momentum distribution of the stripping cross section is given by [13]

$$\begin{aligned}\frac{d\sigma_{\rm str}}{dk_z} = {} & \frac{1}{2\pi} \frac{1}{4\pi} \int d\hat{\boldsymbol{\Omega}} \int d^2\boldsymbol{b}_n [1 - |S_n(\boldsymbol{b}_n)|^2] \int d^2\boldsymbol{\rho} \\ & \times \left| \int dz e^{-ik_z z} S_c(\boldsymbol{b}_c, \hat{\boldsymbol{\Omega}}) \Psi_\omega(\boldsymbol{r}, \hat{\boldsymbol{\Omega}}) \right|^2. \end{aligned} \quad (14)$$

The total cross section of stripping is calculated by integrating over k_z, yielding

$$\begin{aligned}\sigma_{\rm str} = {} & \frac{1}{4\pi} \int d\hat{\boldsymbol{\Omega}} \int d^2\boldsymbol{b}_n [1 - |S_n(\boldsymbol{b}_n)|^2] \\ & \times \int d^3\boldsymbol{r}\, \Psi^*_\omega(\boldsymbol{r}, \hat{\boldsymbol{\Omega}}) |S_c(\boldsymbol{b}_c, \hat{\boldsymbol{\Omega}})|^2 \Psi_\omega(\boldsymbol{r}, \hat{\boldsymbol{\Omega}}). \end{aligned} \quad (15)$$

Another process, elastic breakup or diffraction dissociation, can also be interpreted in terms of survival amplitudes with the help of the eikonal S matrices [13]. Including the effects of deformation, the total cross section for diffraction dissociation is

$$\begin{aligned}\sigma_{\rm diff} = {} & \frac{1}{4\pi} \int d\hat{\boldsymbol{\Omega}} \int d^2\boldsymbol{b}_c \\ & \times \left[\int d^3\boldsymbol{r}\, \Psi^*_\omega(\boldsymbol{r}, \hat{\boldsymbol{\Omega}}) |S_n(\boldsymbol{b}_n) S_c(\boldsymbol{b}_c, \hat{\boldsymbol{\Omega}})|^2 \Psi_\omega(\boldsymbol{r}, \hat{\boldsymbol{\Omega}}) \right. \\ & \left. - \sum_{\omega'} \left| \int d^3\boldsymbol{r}\, \Psi^*_{\omega'}(\boldsymbol{r}, \hat{\boldsymbol{\Omega}}) S_n(\boldsymbol{b}_n) S_c(\boldsymbol{b}_c, \hat{\boldsymbol{\Omega}}) \Psi_\omega(\boldsymbol{r}, \hat{\boldsymbol{\Omega}}) \right|^2 \right]. \end{aligned} \quad (16)$$

One may first assume that the S matrices do not depend on orientation and that deformation effects are solely due to the extended (halo) deformed single-particle wave functions. In this work, we also ignore interference contributions so that the coupled system is diagonal in the $\{l, j\}$ basis. Then the average over all orientations in the cross sections can be simplified by using the orthogonality of the Wigner D

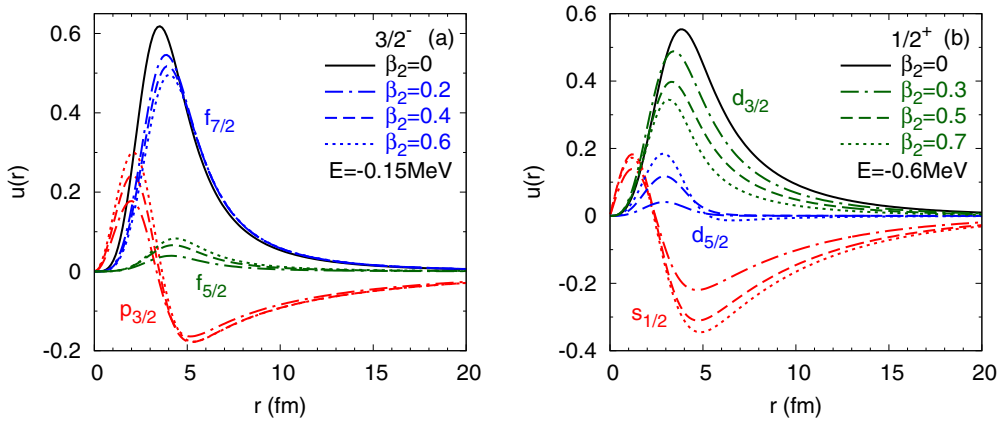

FIG. 1. (a) The channels $p_{3/2}$, $f_{5/2}$, and $f_{7/2}$ in $\Psi_{3/2^-}$. They are compared with the spherical single-particle radial wave function $1f_{7/2}$. (b) The channels $s_{1/2}$, $d_{3/2}$, and $d_{5/2}$ in $\Psi_{1/2^+}$. They are compared with the spherical single-particle radial wave function $1d_{3/2}$.

matrices

$$\int d\phi \int d\theta \sin\theta D^{j*}_{kn}(\phi,\theta,0) D^{j'}_{k'n'}(\phi,\theta,0) = \frac{4\pi}{2j+1}\delta_{jj'}\delta_{kk'}\delta_{nn'}. \quad (17)$$

This method allows us a straightforward use of the longitudinal momentum distribution and the cross sections of stripping and diffraction dissociation as calculated by the MOMDIS code for each $\{l,j\}$ component of the radial wave function and to sum the contributions separately, with the average over orientations for the halo wave function accounted for properly.

In general, the core-target S matrix, $S_c(\boldsymbol{b}_c,\hat{\boldsymbol{\Omega}})$, depends on orientation. Therefore, we have modified the MOMDIS code to include deformation effects in the S matrix or in the eikonal phase as in Eq. (12). We have then proceeded to calculate momentum distributions and cross sections for deformed projectiles following Eqs. (14)–(16). Our results are presented in the next section.

III. RESULTS AND DISCUSSIONS

In this work we are particularly interested in neutron removal from ^{31}Ne projectiles. We consider two possible ground spin-parity states, $3/2^-$ and $1/2^+$, for ^{31}Ne. Following Refs. [12,30], we use the parameters of a deformed Woods-Saxon potential given by $R_0 = R_{SO} = R_C = 3.946$ fm, $a_0 = a_{SO} = 0.67$ fm, and $V_{SO} = -17.33$ MeV.

A. Deformed states in ^{31}Ne

For the quadrupole deformation $\beta_2 = 0.4$ and the effective binding energy $E = -0.15$ MeV, we obtain the following normalized deformed state with spin-parity $3/2^-$:

$$\sum_\alpha u_{\alpha 3/2^-}(r) = \sqrt{0.24}\, p_{3/2}(r) + \sqrt{0.01}\, f_{5/2}(r) + \sqrt{0.75}\, f_{7/2}(r), \quad (18)$$

with $V_0 = -40.0$ MeV. In Fig. 1(a), the dashed lines represent the radial functions of the deformed state, and the solid line is the spherical single-particle radial wave function $1f_{7/2}$ obtained with $\beta_2 = 0$ and an appropriate potential depth V_0

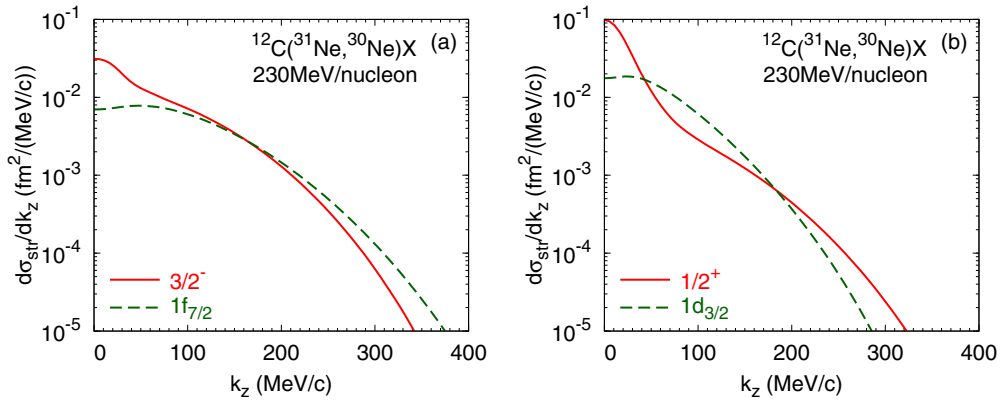

FIG. 2. The longitudinal momentum distribution for ^{12}C(^{31}Ne,^{30}Ne)X at 230 MeV/nucleon. (a) The solid line is for the deformed state $\Psi_{3/2^-}$ with $\beta_2 = 0.4$ and $E = -0.15$ MeV, and the dashed line is for the spherical single-particle wave function $1f_{7/2}$ with the same binding energy. (b) The solid line is for the deformed state $\Psi_{1/2^+}$ with $\beta_2 = 0.6$ and $E = -0.6$ MeV, and the dashed line is for the spherical single-particle wave function $1d_{3/2}$ with the same binding energy.

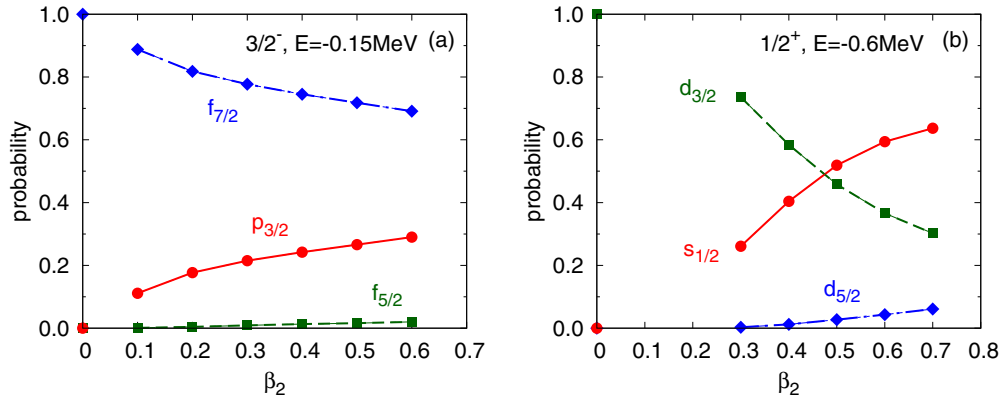

FIG. 3. Squared amplitudes, $\int dr[u_{\alpha\omega}(r)]^2$, for the expansion of the states (a) $\Psi_{3/2^-}$ and (b) $\Psi_{1/2^+}$ in the basis $\alpha = \{l, j\}$.

to reproduce the same binding. We see that the deformation shifts substantial contributions from the $1f_{7/2}$ state to the $2p_{3/2}$ state, at the level of 24%. Because there are uncertainties in the quadrupole deformation parameter and the effective binding energy, we consider the deformed state for several values of β_2 and E. As the deformation decreases, the state $\Psi_{3/2^-}$ approaches the spherical wave function $1f_{7/2}$. It is worth noticing that it is mostly the tail of the wave function ($r \gtrsim 4$ fm) that contributes to nucleon knockout reactions [14]. However, studies with tightly bound nucleons have shown that this is not always true [31].

For $\beta_2 = 0.6$ and $E = -0.6$ MeV, another deformed state with the spin-parity $1/2^+$ can be obtained,

$$\sum_\alpha u_{\alpha 1/2^+}(r) = \sqrt{0.59}s_{1/2}(r) + \sqrt{0.37}d_{3/2}(r) + \sqrt{0.04}d_{5/2}(r), \quad (19)$$

with the potential depth $V_0 = -38.1$ MeV. In Fig. 1(b) we show that the state $\Psi_{1/2^+}$ approaches the spherical $1d_{3/2}$ state as $\beta_2 \to 0$. Deformation drains the contribution of the $1d_{3/2}$ state to the $2s_{1/2}$ state and makes their amplitudes nearly similar in strength.

B. Nucleon knockout from ^{31}Ne

We now consider the single-neutron removal reaction ^{12}C(^{31}Ne,^{30}Ne)X at the laboratory energy of 230 MeV per nucleon. The nucleon-nucleon scattering parameters $\alpha_{NN} = 0.73$, $\beta_{NN} = 0.58$, and $\sigma_{NN} = 3.02$ fm^2 are used [24,25]. The intrinsic matter density of the neutron (or proton), $\rho(r)$, is taken as a Gaussian function, corresponding to a form factor, $\rho(q) = C\exp(-a^2q^2/4)$. We use $a = 0.7$ fm for a nucleon density rms radius of 0.86 fm. The density rms radii of the core and target are 3.69 and 2.90 fm, respectively. For the core we have used a liquid-drop model density [29], and for the carbon target we have used the density parametrization taken from Ref. [32]. We have verified that using a core density based on a Hartree-Fock-Bogoliubov calculation with the SLy5 Skyrme interaction does not change our results in a noticeable way. On the other hand, Ref. [20] (see their Fig. 5) has shown that cross sections have some sensitivity to the relative sizes of the core and the neutron wave function.

In Fig. 2, we plot the calculated longitudinal momentum distributions of the two deformed states (solid lines) and compare with the distributions obtained using the spherical single-particle wave functions (dashed lines). Near $k_z = 0$, the cross sections obtained with the deformed states are larger than those obtained with the spherical wave functions. We note that the width of the momentum distribution changes with projectile deformation. This is expected because the $p_{3/2}$ state and the $s_{1/2}$ state [in Eqs. (18) and (19)] have different, less space confining, centrifugal barriers than the corresponding $f_{7/2}$ and $d_{3/2}$ states, respectively. Therefore, admixture with the $p_{3/2}$ state and the $s_{1/2}$ state will induce narrower momentum distributions due to a larger spatial extension of the wave functions. In fact, the spatial extension (the rms radius) of the deformed states is larger than that of the spherical waves. In summary, we expect the deformed states to produce larger cross sections at low momentum and narrower momentum distributions in comparison with the spherical waves.

To investigate the core deformation effects, we have obtained the solutions with different values of the deformation parameter β_2 for fixed energy E. All the parameters of the Woods-Saxon potential are fixed while the central potential depth is adjusted so that the energy E of the state with β_2 is reproduced. Depending on β_2, each shell occupation amplitude in Eqs. (18) and (19) changes and so do their wave functions, as displayed in Fig. 1 (see also Fig. 3). The rms radius of the

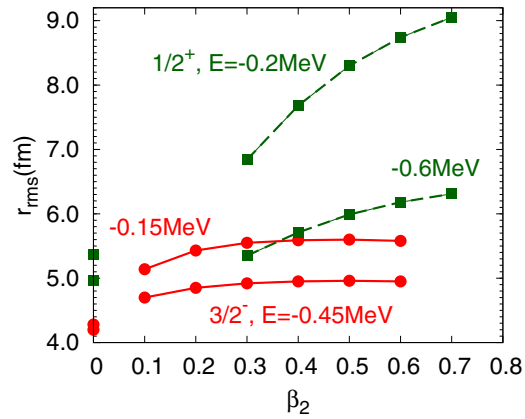

FIG. 4. The wave functions' rms radii.

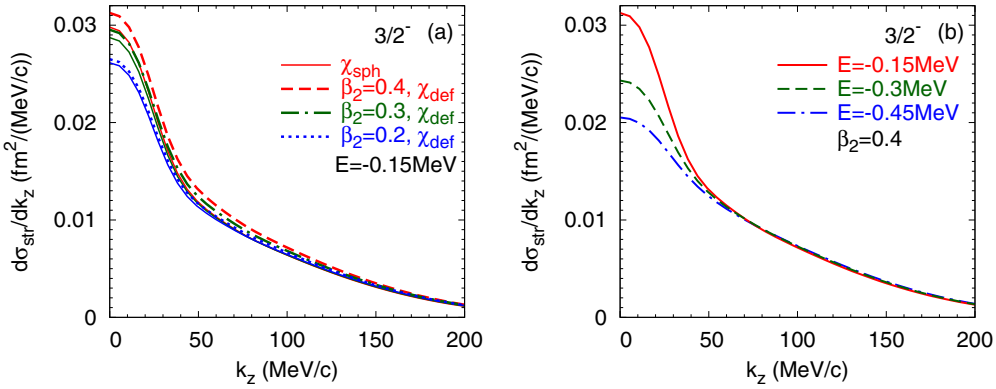

FIG. 5. Longitudinal momentum distributions of core fragments from neutron knockout from the deformed state $\Psi_{3/2^-}$. (a) The dependence on the quadrupole deformation is displayed. The dashed, dash-dotted, and dotted lines represent the calculated results using Eq. (12). The solid lines are for the results obtained with Eq. (9). (b) The dependence on the effective binding energy of the valence neutron is shown.

deformed states, $r_{\rm rms} = [\sum_\alpha \int dr\, [u_{\alpha\omega}(r)]^2 r^2]^{1/2}$, is shown in Fig. 4. We note that $r_{\rm rms}$ increases with deformation for fixed E for reasons explained above.

In Figs. 5(a) and 6(a), we present the dependence of the calculated longitudinal momentum distributions on projectile deformation. The calculated results using the orientation-dependent core-target S matrix, Eq. (12), are compared with the results using the spherical S matrix, Eq. (9). With the deformed phase, the total cross section increases by 2%–11% compared with the spherical phase. The effect of the deformed phase is pronounced near $k_z = 0$ for strong deformation. As expected from the relation between $r_{\rm rms}$ and deformation (Fig. 4), the stronger the quadrupole deformation is, the larger cross section we obtain.

Similarly, in Figs. 5(b) and 6(b), we have calculated the momentum distributions depending on E for fixed β_2. The $r_{\rm rms}$ decreases as $|E|$ increases, which is reflected in the cross sections. We observe that the widths of momentum distributions are sensitive to the effective binding energy of the valence neutron, as in the spherical case. Smaller widths are associated with smaller binding due to the larger extension of the wave function. They are also influenced by the angular momentum l content of the deformed state.

Evidently, the cross sections increase with the rms radii of deformed states. This result contrasts with those reported in Ref. [20] where no correlation between the cross sections and the rms radii of the Nilsson states has been found. In Fig. 7, we present the average l value, $\langle l\rangle = \sum_\alpha l_\alpha \int dr [u_{\alpha\omega}(r)]^2$, as a function of β_2 and E. As the quadrupole deformation grows, $\langle l\rangle$ decreases. This is because the probability of the $f_{7/2}$ ($d_{3/2}$) component in the state $\Psi_{3/2^-}$ ($\Psi^+_{1/2}$) decreases while that of $p_{3/2}$ ($s_{1/2}$) increases (see Fig. 3). As the core mean-field deformation changes, the occupation probabilities of spherical orbitals redistribute. Therefore, the cross sections and the widths of the corresponding momentum distributions change appreciably with deformation. When the binding energy grows, the probability of each channel changes in the opposite way. If the opposite behavior would increase $\langle l\rangle$ with $|E|$, then the cross section would display an inverse trend with the average l value. We note that the widths of longitudinal momentum distributions increase with the average l value. Although our deformed states show different behaviors with the rms radii from the Nilsson states, the dependence of the cross sections and momentum distributions on $\langle l\rangle$ obtained with our method is similar to the results reported in Ref. [20].

For prolate projectile deformation, the cross section is expected to be the largest when the symmetry axis is perpendicular to the beam axis and the smallest when parallel. This behavior is shown in Fig. 8 where we present our calculations for neutron removal cross sections as a function of the Euler

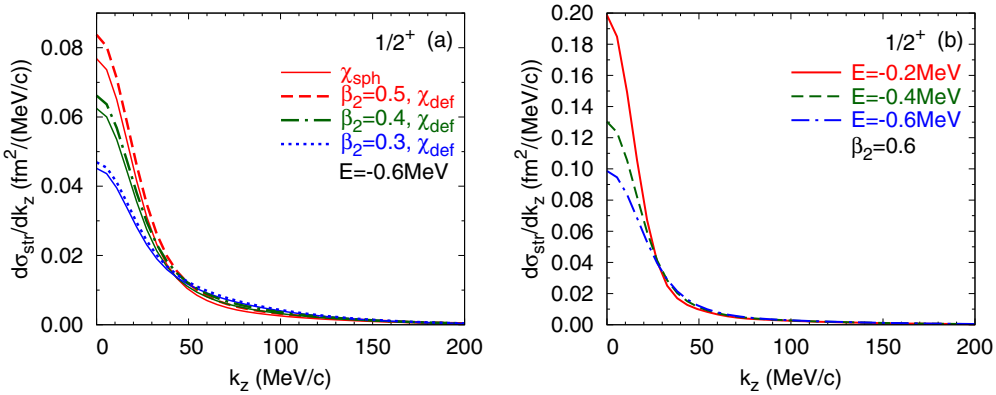

FIG. 6. Same as Fig. 5 but for the deformed state $\Psi_{1/2^+}$.

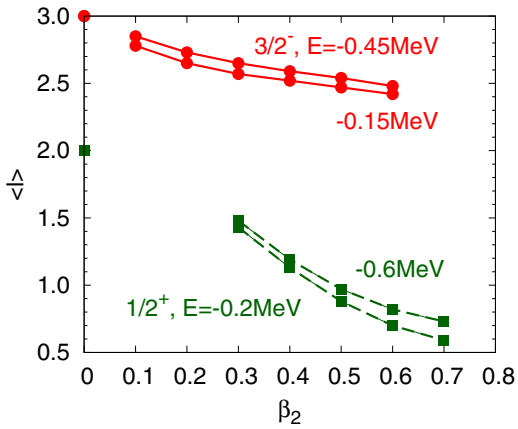

FIG. 7. The average l values of the states $\Psi_{3/2^-}$ and $\Psi_{1/2^+}$.

angle θ_o of the core symmetry axis. The distributions calculated with the deformed eikonal phase are compared with those with the spherical phase. In contrast to momentum distributions, we find that orientation distributions are sensitive to the orientation dependence of the core-target S matrix. Depending on deformation, the core density in Eq. (10) changes with the angle θ_o. The density has the maximum value at $\theta_o = \pi/2$ and the minimum at $\theta_o = 0$. Thus, the cross sections calculated with the deformed phase are larger (smaller) than the cross sections with the spherical phase near $\theta_o = \pi/2$ ($\theta_o = 0$). The deformation effects grow with β_2.

According to our calculations, Fig. 9 shows the total cross sections of stripping and diffraction dissociation. Both stripping and diffraction cross sections increase with quadrupole deformation. The total cross section of diffraction dissociation amounts to 15%–19% of that of stripping.

In Fig. 10, we present the sum of stripping and diffraction cross sections depending on β_2 and E. The sum of cross sections for the normalized deformed states [Eqs. (18) and (19)] can be compared with the measured cross section feeding the ground state of the residual core, $\sigma^{\rm gs}_{\rm exp} = 3.3(1.5)$ fm^2 [33]. $\sigma_{\rm str+diff}$ of $\Psi_{3/2^-}$ is comparable to $\sigma^{\rm gs}_{\rm exp}$ while that of $\Psi_{1/2^+}$ is larger than the measured one unless $\beta_2 \lesssim 0.3$.

We expect that once the spectroscopic factors are specified, one can use the calculated cross sections and momentum distributions to deduce the spin-parity state of ^{31}Ne and to determine the accurate values of β_2 and E. In Ref. [33], the experimental partial cross sections feeding the ground core state and excited core states have been determined. The neutron removal of the halo neutron from ^{31}Ne is expected to produce the core in its ground state. On the other hand, if the core is produced in an excited state, the removed neutron is likely to be one of the nonhalo neutrons from the core ^{30}Ne. Indeed, the cross section for populating excited core states $[\sigma^{\rm inc}_{\rm exp} - \sigma^{\rm gs}_{\rm exp} = 90(7) - 33(15)$ mb] is similar to that of neutron removal from ^{30}Ne [62(2) mb at 228 MeV/nucleon] [34].

Our calculations in the above are for knockout reactions of the halo neutron from ^{31}Ne, populating the ground state of the deformed core. For producing excited core states, we can consider neutron removal from the core ^{30}Ne. To compare with inclusive (populating both ground and excited core states) momentum distributions, we include spherical calculations for neutron removal from ^{30}Ne and add them to the ground-state calculations (see Fig. 11). For excited states of the residue, the neutron configurations of $2p_{3/2}$ and $1f_{7/2}$ are considered with the spectroscopic factors of 0.34 and 0.80 [33], respectively, in the case of the deformed state $\Psi_{3/2^-}$. For the state $\Psi_{1/2^+}$, $1d_{3/2}$ is considered with the spectroscopic factor 0.55 [33].

We mention that our approach has some limitations to analyze the cross sections populating excited core states. The cross sections of excited core states are independent of β_2 and their (especially f and d configurations) dependencies on E are relatively weaker than those of the ground core states. In addition, the cross sections are not exclusively determined by experimental measurements, and we can compare only the sum of cross sections for both ground and excited core states with data. As a result, the comparison of the inclusive cross sections calculated in our method with experimental data is somewhat subtle.

The comparisons of the ground-state cross section (Fig. 10) and the inclusive cross section (Fig. 11) with experimental data can be useful to investigate the possible ranges of β_2 and E. As discussed above, the dependencies of the inclusive cross section on β_2 and E are less clear though. For $0.3 \lesssim \beta_2 \lesssim 0.5$, $\sigma^{\rm gs}_{\rm str+diff}$ and $\sigma^{\rm inc}_{\rm str+diff}$ of $\Psi_{3/2^-}$ agree with experimental data if 0.3 MeV $\lesssim |E| \lesssim 0.45$ MeV. For $\beta_2 \approx 0.2$, the theoretical predictions with 0.15 MeV $\lesssim |E| \lesssim 0.3$ MeV are comparable to the

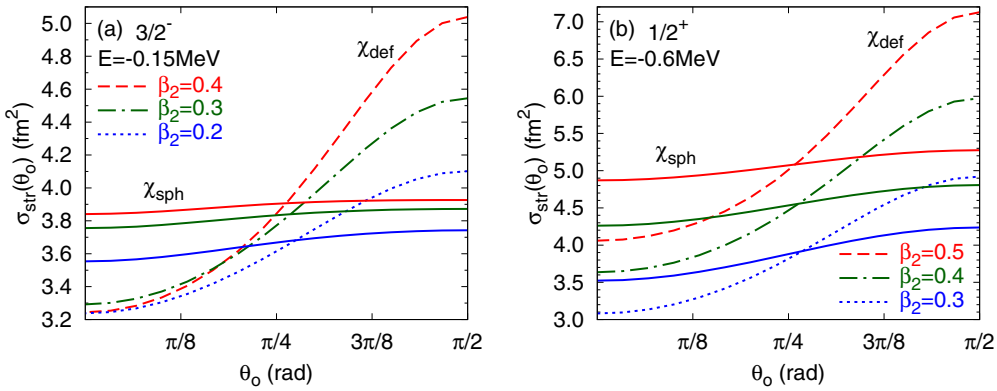

FIG. 8. Neutron knockout cross sections as a function of the Euler angle θ_o of the core symmetry axis for the states (a) $\Psi_{3/2^-}$ and (b) $\Psi_{1/2^+}$. The solid lines are calculated with Eq. (9), and the dashed, dash-dotted, and dotted lines are calculated with Eq. (12).

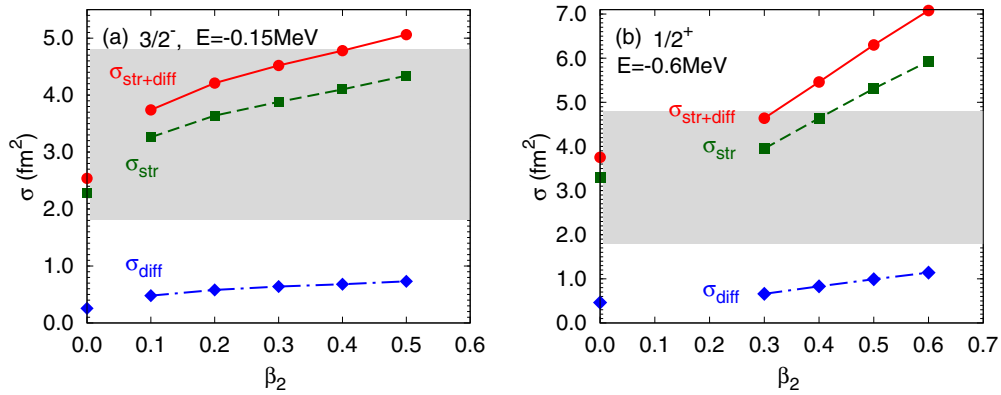

FIG. 9. Stripping, diffraction dissociation, and the sum of the two cross sections for the deformed states (a) $\Psi_{3/2^-}$ and (b) $\Psi_{1/2^+}$. The shaded region represents the measured cross section feeding the ground state of the residual core, $\sigma^{\rm gs}_{\rm exp} = 3.3(1.5)$ fm^2 [33]. The experimental uncertainty is represented by the width of the shaded region.

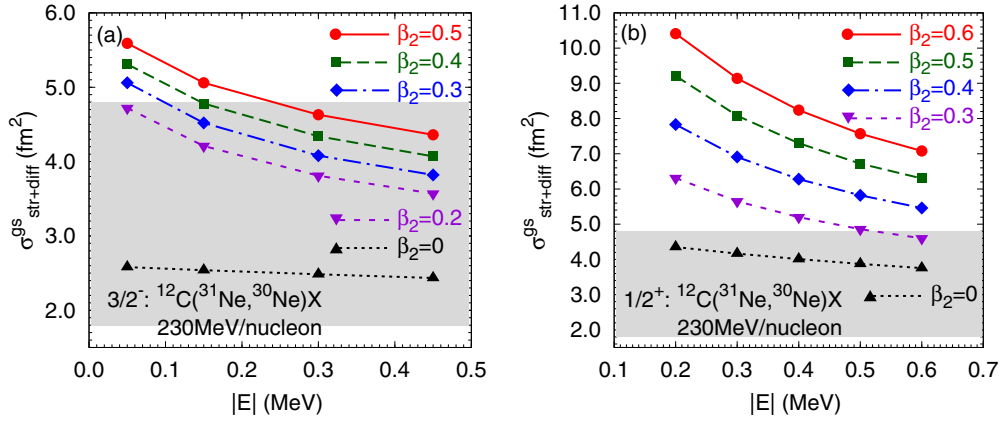

FIG. 10. The sum of stripping and diffraction cross sections for the deformed states (a) $\Psi_{3/2^-}$ and (b) $\Psi_{1/2^+}$. The shaded region represents the measured cross section feeding the ground state of the residual core, $\sigma^{\rm gs}_{\rm exp} = 3.3(1.5)$ fm^2 [33].

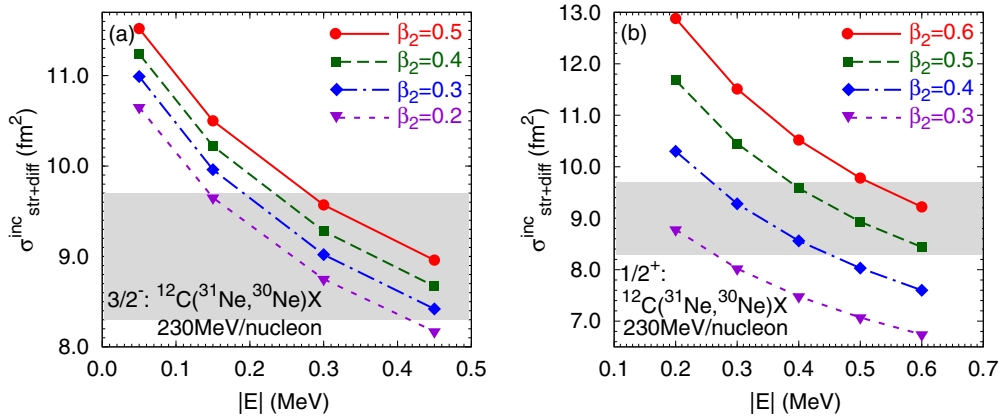

FIG. 11. The inclusive cross sections for the deformed states (a) $\Psi_{3/2^-}$ and (b) $\Psi_{1/2^+}$. The shaded region represents the experimental inclusive cross section, $\sigma^{\rm inc}_{\rm exp} = 9.0(0.7)$ fm^2 [33].

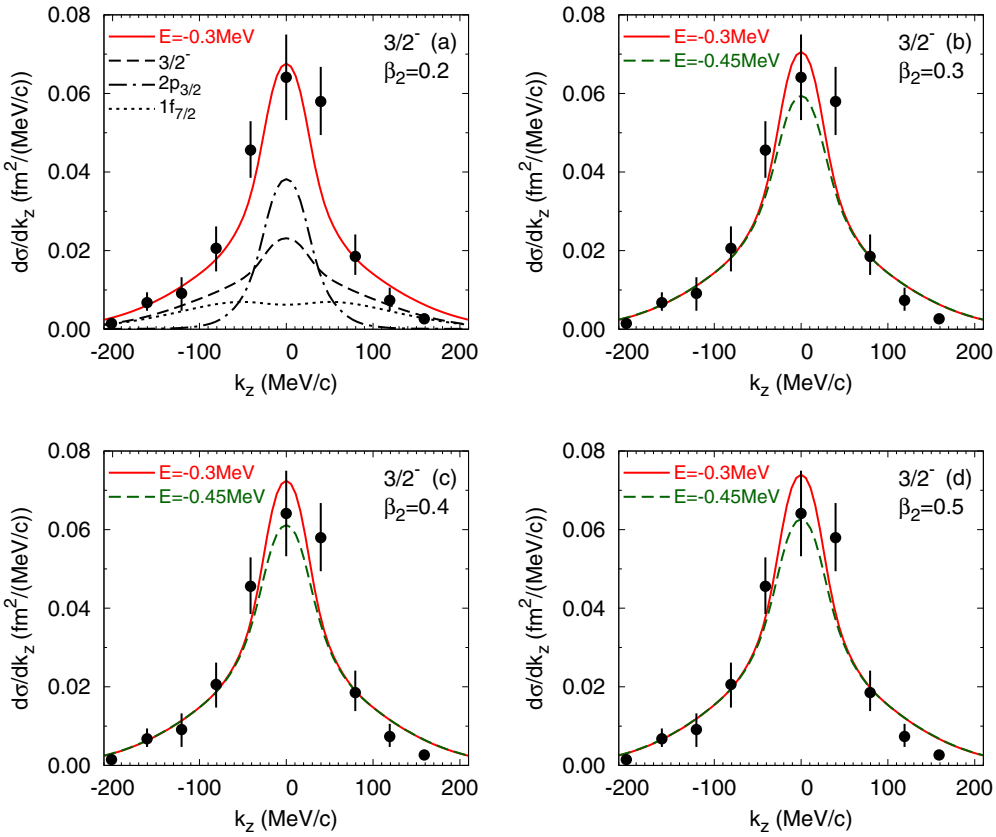

FIG. 12. The inclusive longitudinal momentum distribution for the deformed state $\Psi_{3/2^-}$. In panel (a), the valence neutron contributions from $\Psi_{3/2^-}$, $2p_{3/2}$, and $1f_{7/2}$ are shown as the dashed, dashed-dotted, and dotted line, respectively. The circles with error bars represent the inclusive one-neutron removal cross sections [33].

measured ones. On the other hand, $\sigma^{\rm gs}_{\rm str+diff}$ of $\Psi^+_{1/2}$ with strong deformation is larger, but $\sigma^{\rm inc}_{\rm str+diff}$ with weak deformation and strong binding is smaller than experimental data.

Figures 12 and 13 show the comparison of the inclusive momentum distributions with experimental data. In Fig. 12(a), the partial cross sections feeding the ground $(3/2^-)$ core state and the excited $(2p_{3/2}$ and $1f_{7/2})$ core states are shown as styled lines. The solid line represents the sum of all the contributions and is compared with the data. For $\beta_2 = 0.2$, the inclusive momentum distribution with $E = -0.3$ MeV agrees with the experimental data. However, the momentum distribution with larger (smaller) $|E|$ is wider (narrower) than the measured one. For $0.3 \lesssim \beta_2 \lesssim 0.5$, the momentum distributions are comparable if 0.3 MeV $\lesssim |E| \lesssim$ 0.45 MeV. The inclusive longitudinal momentum distributions are not very sensitive to deformation except near $k_z = 0$. Especially, the results in Figs. 12(b), 12(c), and 12(d) exhibit almost the same widths for each $E = -0.3$ and -0.45 MeV. On the other hand, the longitudinal momentum distributions of the deformed state $\Psi_{1/2^+}$ do not agree with the experimental data. Figure 13 shows the momentum distribution with $\beta_2 = 0.4$, but for stronger deformation (which is suggested by Ref. [12]) the distributions become narrower.

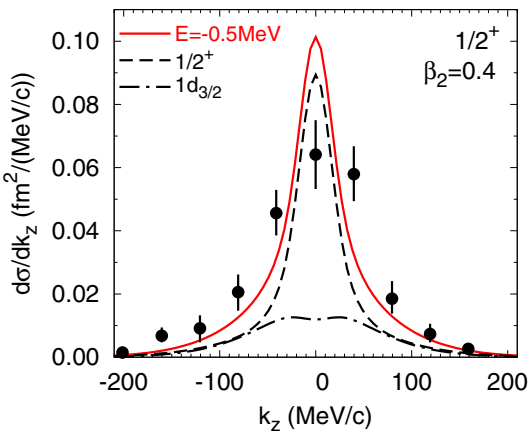

FIG. 13. Same as Fig. 12 but for the deformed state $\Psi_{1/2^+}$. The valence neutron contributions from $\Psi_{1/2^+}$ and $1d_{3/2}$ are shown as the dashed and dashed-dotted lines, respectively.

The calculated momentum distributions of the state $\Psi_{3/2^-}$ have the full width at half maximum, approximately 82–93 MeV/c, and they are narrower at low momentum and broader at high momentum than the measured one. The width of the measured momentum distribution is 77(18) MeV/c, extracted from a Lorentzian fit [33]. In the contribution of the ground state of the residue, we have not included interference contributions, which might account for the difference between our results and experimental data.

For $\beta_2 = 0.5$ and $E = -0.15$ MeV, the probabilities for reactions through the channels $p_{3/2}$, $f_{5/2}$, and $f_{7/2}$ in Fig. 3(a) are close to those in Fig. 3(b) of Ref. [12]. The deformed state $\Psi_{3/2^-}$ seems to have a good correspondence with the Nilsson level [321 3/2].

IV. SUMMARY

Using the Glauber model for knockout reactions, we have studied the one-neutron removal reaction from the deformed projectile ^{31}Ne incident on carbon targets at 230 MeV/nucleon. We have generated single-particle wave functions with a deformed Woods-Saxon potential to calculate longitudinal momentum distributions using an orientation-dependent core-target S matrix. The calculated longitudinal momentum distributions and cross sections have been analyzed with a quadrupole deformation parameter and an effective binding energy of the valence neutron.

We observe that the cross section for the reaction increases with the wave function rms radius of the deformed states and has the inverse trend to the average l value. This trend is meaningful based on the interpretation of the role of the centrifugal barrier. The width of the momentum distribution is also sensitive to the effective binding energy of the valence neutron, as it determines the extension of the single particle states.

Our major conclusions are as follows. The sum of stripping and diffraction cross sections of the normalized state $\Psi_{3/2^-}$ is comparable with the measured cross section feeding the ground state of the residue. By including the neutron removal from the core with the neutron configurations p and f, the inclusive momentum distribution and the total cross section for $\beta_2 \approx 0.2$ and $0.3 \lesssim \beta_2 \lesssim 0.5$ agree with experimental data if $|E| \approx 0.3$ MeV and 0.3 MeV $\lesssim |E| \lesssim 0.45$ MeV, respectively. We mention that the inclusive longitudinal momentum distribution is not very sensitive to deformation at least for $\beta_2 = 0.3$–0.5. By including spherical calculations for excited core states, the dependencies of the total cross sections and the longitudinal momentum distributions on β_2 and E become weaker than those of the ground core states. In that respect, our approach has some subtleties to analyze the total inclusive cross sections. Our result, nevertheless, is consistent with the analysis of Refs. [12] and [33] in which a small neutron separation energy of $S_n = 0.15^{+0.16}_{-0.10}$ MeV is obtained (the measured one $S_n = 0.29 \pm 1.64$ MeV [35] contains large uncertainties). On the other hand, the cross sections of $\Psi_{1/2^+}$ are larger and the widths of their corresponding momentum distributions are narrower than experimental data unless the core is weakly deformed (which disagrees with Ref. [12]).

Our results indicate that ^{31}Ne has the spin-parity $3/2^-$. With exclusive experimental measurements of cross sections and momentum distributions for both ground and excited core states, our method can be used further to study the spin-parity state of deformed nuclei, and the effects of deformation and binding energies, on nucleon removal reactions.

ACKNOWLEDGMENTS

This work is supported by the Rare Isotope Science Project of the Institute for Basic Science funded by the Ministry of Science, ICT and Future Planning and the National Research Foundation of Korea (Grant No. 2013M7A1A1075764). C.A.B. acknowledges support under U.S. DOE Grant No. DDE-FG02-08ER41533 and U.S. NSF Grant No. PHY-1415656. A.K. acknowledges funding support from Hungarian Scientific Research Fund OTKA Grant No. K112962.

APPENDIX: THE EIKONAL PHASE FOR QUADRUPOLE DEFORMED CORE

In the second term of Eq. (11),

$$\frac{1}{2\pi}\int d^2\boldsymbol{q}\,\rho_t(q) f_{NN}(q)\, e^{-i(\boldsymbol{b}-\boldsymbol{\rho})\cdot\boldsymbol{q}} = \frac{1}{2\pi}\int dq\, q\rho_t(q) f_{NN}(q)\int d\phi_q\, e^{-i|\boldsymbol{b}-\boldsymbol{\rho}|q\cos\phi_q},$$
$$= \int dq\, q\rho_t(q) f_{NN}(q) J_0(|\boldsymbol{b}-\boldsymbol{\rho}|q). \tag{A1}$$

Using the Graf's addition theorem [36],

$$J_0(\sqrt{x^2+y^2-2xy\cos\phi}) = \sum_n J_n(x)J_n(y)e^{in\phi}, \tag{A2}$$

we have

$$\frac{1}{2\pi}\int d^2\boldsymbol{q}\,\rho_t(q) f_{NN}(q) e^{-i(\boldsymbol{b}-\boldsymbol{\rho})\cdot\boldsymbol{q}} = \int dq q\rho_t(q) f_{NN}(q)\sum_n J_n(qb)J_n(q\rho)e^{in\phi}. \tag{A3}$$

Then, for the quadrupole deformed core, the second term of Eq. (11) becomes

$$\sum_m R_0\beta_2 D^2_{m0}(\hat{\boldsymbol{\Omega}})\int d^3\boldsymbol{r}\, Y_{2m}(\hat{\boldsymbol{r}})\frac{\partial\rho_c}{\partial r}\bigg|_{\beta_2=0}\frac{1}{2\pi k_{NN}}\int d^2\boldsymbol{q}\,\rho_t(q) f_{NN}(q) e^{-i(\boldsymbol{b}-\boldsymbol{\rho})\cdot\boldsymbol{q}}$$
$$= \sum_m \frac{1}{k_{NN}} R_0\beta_2 D^2_{m0}(\hat{\boldsymbol{\Omega}})\int dr r^2\int d\theta\sin\theta\int d\phi Y_{2m}(\hat{\boldsymbol{r}})\frac{\partial\rho_c}{\partial r}\bigg|_{\beta_2=0}\int dq q\rho_t(q) f_{NN}(q)\sum_n J_n(qb)J_n(q\rho)e^{in\phi}. \tag{A4}$$

By integrating over ϕ and θ, Eq. (A4) becomes

$$\sum_m \sqrt{\frac{(2-m)!}{(2+m)!}}\frac{\sqrt{5\pi}}{k_{NN}} R_0\beta_2 D^2_{m0}(\hat{\mathbf{\Omega}}) \int dr r^2 \int d\theta \sin\theta P_2^m(\cos\theta)\frac{\partial\rho_c}{\partial r}\bigg|_{\beta_2=0} \int dq q\rho_t(q) f_{NN}(q) J_{-m}(qb) J_{-m}(qr\sin\theta)$$
$$= \frac{\sqrt{5\pi}}{k_{NN}} R_0\beta_2 D^2_{00}(\hat{\mathbf{\Omega}}) \int dr \frac{\partial\rho_c}{\partial r}\bigg|_{\beta_2=0} \int dq J_0(qb)\rho_t(q) f_{NN}(q)\frac{1}{q^2 r}[(3-q^2r^2)\sin(qr) - 3qr\cos(qr)] + \sqrt{\frac{15\pi}{2}}\frac{1}{k_{NN}}$$
$$\times R_0\beta_2\left[D^2_{20}(\hat{\mathbf{\Omega}}) + D^2_{-20}(\hat{\mathbf{\Omega}})\right] \int dr \frac{\partial\rho_c}{\partial r}\bigg|_{\beta_2=0} \int dq J_2(qb)\rho_t(q) f_{NN}(q)\frac{1}{q^2 r}[(3-q^2r^2)\sin(qr) - 3qr\cos(qr)]. \quad \text{(A5)}$$

[1] T. Nakamura *et al.*, Phys. Rev. Lett. **103**, 262501 (2009).
[2] A. Poves and J. Retamosa, Nucl. Phys. A **571**, 221 (1994).
[3] P. Descouvemont, Nucl. Phys. A **655**, 440 (1999).
[4] K. Minomo, T. Sumi, M. Kimura, K. Ogata, Y. R. Shimizu, and M. Yahiro, Phys. Rev. C **84**, 034602 (2011).
[5] T. Sumi, K. Minomo, S. Tagami, M. Kimura, T. Matsumoto, K. Ogata, Y. R. Shimizu, and M. Yahiro, Phys. Rev. C **85**, 064613 (2012).
[6] K. Minomo, T. Sumi, M. Kimura, K. Ogata, Y. R. Shimizu, and M. Yahiro, Phys. Rev. Lett. **108**, 052503 (2012).
[7] W. Horiuchi, Y. Suzuki, P. Capel, and D. Baye, Phys. Rev. C **81**, 024606 (2010).
[8] Y. Urata, K. Hagino, and H. Sagawa, Phys. Rev. C **83**, 041303(R) (2011).
[9] Y. Urata, K. Hagino, and H. Sagawa, Phys. Rev. C **86**, 044613 (2012).
[10] M. Takechi *et al.*, Phys. Lett. B **707**, 357 (2012).
[11] Shubhchintak and R. Chatterjee, Nucl. Phys. A **922**, 99 (2014).
[12] I. Hamamoto, Phys. Rev. C **81**, 021304(R) (2010).
[13] K. Hencken, G. Bertsch, and H. Esbensen, Phys. Rev. C **54**, 3043 (1996).
[14] P. G. Hansen and J. A. Tostevin, Annu. Rev. Nucl. Part. Sci. **53**, 219 (2003).
[15] C. A. Bertulani and A. Gade, Comput. Phys. Commun. **175**, 372 (2006).
[16] C. A. Bertulani and P. G. Hansen, Phys. Rev. C **70**, 034609 (2004).
[17] A. Sakharuk and V. Zelevinsky, Phys. Rev. C **61**, 014609 (1999).
[18] J. A. Christley and J. A. Tostevin, Phys. Rev. C **59**, 2309 (1999).
[19] P. Batham, I. J. Thompson, and J. A. Tostevin, Phys. Rev. C **71**, 064608 (2005).
[20] E. C. Simpson and J. A. Tostevin, Phys. Rev. C **86**, 054603 (2012).
[21] G. Singh, Shubhchintak, and R. Chatterjee, Phys. Rev. C **94**, 024606 (2016).
[22] H. Esbensen, Phys. Rev. C **53**, 2007 (1996).
[23] C. A. Bertulani and P. Danielewicz, *Introduction to Nuclear Reactions* (IOP, Bristol, UK, 2004).
[24] M. S. Hussein, R. A. Rego, and C. A. Bertulani, Phys. Rep. **201**, 279 (1991).
[25] L. Ray, Phys. Rev. C **20**, 1957 (1979).
[26] M. S. Hussein and K. W. McVoy, Nucl. Phys. A **445**, 124 (1985).
[27] A. T. Kruppa and Z. Papp, Comput. Phys. Commun. **36**, 59 (1985).
[28] P. J. Moffa, C. B. Dover, and J. P. Vary, Phys. Rev. C **16**, 1857 (1977).
[29] W. D. Myers, Nucl. Phys. A **145**, 387 (1970).
[30] A. Bohr and B. R. Mottelson, *Nuclear Structure* (Benjamin, Reading, MA, 1969), Vol. I.
[31] A. Gade, P. Adrich, D. Bazin, M. D. Bowen, B. A. Brown, C. M. Campbell, J. M. Cook, T. Glasmacher, P. G. Hansen, K. Hosier, S. McDaniel, D. McGlinchery, A. Obertelli, K. Siwek, L. A. Riley, J. A. Tostevin, and D. Weisshaar, Phys. Rev. C **77**, 044306 (2008).
[32] H. De Vries, C. W. De Jager, and C. De Vries, At. Data Nucl. Data **36**, 495 (1987).
[33] T. Nakamura *et al.*, Phys. Rev. Lett. **112**, 142501 (2014).
[34] H. N. Liu *et al.*, Phys. Lett. B **767**, 58 (2017).
[35] B. Jurado *et al.*, Phys. Lett. B **649**, 43 (2007).
[36] M. Abramowitz and I. A. Stegun, *Handbook of Mathematical Functions* (Dover Publications, New York, 1964).